

# Camera-Based Neonatal Blood Pressure Estimation From Multisite and Multiwavelength Pulse Transit Time—A Proof of Concept in NICU

Yongshen Zeng<sup>id</sup>, Yingen Zhu<sup>id</sup>, Xiaoyan Song<sup>id</sup>, Qiqiong Wang<sup>id</sup>, Jie Yang, and Wenjin Wang<sup>id</sup>

**Abstract**—Blood pressure (BP) is a vital physiological parameter for early warning and prompt intervention treatment in the neonatal intensive care unit (NICU). However, the application of contactless BP measurement methods in neonates remains under-explored. This proof-of-concept clinical study proposes using multisite and multiwavelength pulse transit time (PTT) generated from remote-Photoplethysmography (rPPG) for neonatal BP estimation. A dataset of 40 neonates was created in the NICU under three alternating phases (resting - BP measurement - resting). The spatially averaged rPPG signals from five body parts were used to calculate multiple PTT features, including multisite PTT (MS-PTT) derived from different body parts and multiwavelength PTT (MW-PTT) derived from different skin layers, for BP estimation. Three machine learning models, including multivariate linear regression (MLR), support vector regression (SVR), and random forest regression (RFR), were employed for both univariate and multivariate regression. Combining MS-PTT and MW-PTT yielded the best results, achieving a mean absolute error  $\pm$  standard deviation ( $MAE \pm STD$ ) of  $7.65 \pm 7.48$  mmHg for SBP,  $6.31 \pm 5.58$  mmHg for DBP, and  $7.29 \pm 7.29$  mmHg for MBP, based on MLR with subject-dependent modeling. According to the British Hypertension Society guidelines, these results meet the requirements for Grade C. These findings provide the first clinical proof-of-concept of using camera-based MS-PTT and MW-PTT features for contactless neonatal BP estimation.

**Index Terms**—Blood pressure (BP) estimation, camera-based monitoring, neonatal intensive care unit (NICU), premature neonates, pulse transit time (PTT).

## I. INTRODUCTION

BLOOD pressure (BP) is a vital indicator of cardiovascular function and a key parameter for monitoring neonatal hemodynamics. During the early neonatal period, the

Received 15 February 2025; revised 23 March 2025; accepted 26 March 2025. Date of publication 4 April 2025; date of current version 27 June 2025. This work was supported in part by the National Key Research and Development Program of China under Grant 2022YFC2407800; in part by the National Natural Science Foundation of China under Grant 62271241 and Grant 6235006; in part by the Guangdong Basic and Applied Basic Research Foundation under Grant 2023A1515012983; in part by the Shenzhen Science and Technology Program under Grant JSGGKQTD20221103174704003; and in part by the Shenzhen Fundamental Research Program under Grant JCYJ20220530112601003. (Corresponding author: Wenjin Wang.)

Yongshen Zeng, Yingen Zhu, and Wenjin Wang are with the Department of Biomedical Engineering, Southern University of Science and Technology, Shenzhen 518055, China (e-mail: wangwj3@sustech.edu.cn).

Xiaoyan Song, Qiqiong Wang, and Jie Yang are with the Neonatal Intensive Care Unit, Nanfang Hospital of Southern Medical University, Guangzhou 510515, China.

Digital Object Identifier 10.1109/JIOT.2025.3557771



Fig. 1. Cuff-based neonatal BP monitoring in NICU. BP cuffs are difficult to match in size, and prolonged cuff compression may influence limb circulations. Cameras enable noncontact measurement of neonatal vital signs, including BP.

transition from fetal to adult circulation involves significant hemodynamic changes, such as increased pulmonary blood flow, umbilical vessel closure, and reduced pulmonary vascular resistance. These changes can cause BP fluctuations, potentially leading to organ ischemia, hypoxia, or functional impairment [1]. Preterm infants are particularly vulnerable to abnormal BP fluctuations due to factors like hypoxia, infections, and circulatory issues, increasing the risk of complications, such as intracranial hemorrhage and periventricular leukomalacia [2]. Thus, accurate BP monitoring is essential for preventing severe complications and guiding treatment in critically ill neonates.

In recent years, the integration of camera-based technology into IoT ecosystems has shown great promise in biomedical applications. Studies have also shown that video-based CCTV systems can monitor physiological parameters like heart rate (HR) and respiratory rate (RR) [3], and patient behaviors, such as movement, posture, and actigraphy. Combined with machine learning algorithms, they allow real-time health assessment. Edge computing enables on-device processing for immediate responses, while cloud computing supports large-scale data storage, more advanced analytics, and long-term modeling of patient well-being. These capabilities highlight the critical role of camera-based IoT in advancing the Internet of Medical Things (IoMT). As IoMT drives AI-powered hospitals and smart patient management, our work demonstrates how these technologies enable noncontact, real-time patient monitoring, paving the way for the development of intelligent healthcare systems.

In NICU, neonatal BP is measured using two main methods. Invasive techniques provide continuous and precise monitoring, especially for critically ill infants, but carry risks of infection and bleeding [4]. Noninvasive methods are less intrusive and safer but can be affected by factors like excessive movement, improper cuff size (e.g., a cuff width-to-arm circumference ratio of 0.45 to 0.55 is recommended for preterm infants [5]), and prolonged compression which can cause local ischemia (as shown in Fig. 1). Cuffless NIBP monitoring offers key advantages for neonates, particularly in comfort and continuous measurement. Methods using Electrocardiogram (ECG) and Photoplethysmography (PPG) sensors to measure pulse arrival time (PAT) have been explored (as shown in Table I) [6], [7], [8], [9], [10]. However, ECG electrodes may not be suitable for neonates with allergies or burns.

Cameras have been used for monitoring the physiological states of neonates in NICU, including the measurement of HR [26], HRV [27], SpO<sub>2</sub> [28], [29], RR [30], [31], discomfort [32], [33], and sleep status [34], [35]. Although multiple vital signs are measured, BP still remains to be explored. Using the camera-based method to extract two remote photoplethysmography (rPPG) signals from different body parts or different skin depths has shown potential for contactless BP monitoring [20], [23], [36]. While rPPG using camera technology is gaining popularity for monitoring BP among adults, its research on neonates is limited due to the difficulty in obtaining neonatal BP data in clinics. Compared to adults, neonates have a significantly lower BP range, more delicate and thinner skin, weaker pulsatility (low perfusion index), and an underdeveloped cardiovascular system. These differences make it more difficult to measure reliable BP data from neonates. This study aims to investigate the feasibility of using the rPPG technology to estimate the BP of neonates.

This study proposes a contactless method for neonatal BP estimation using rPPG signals. pulse transit time (PTT) features were extracted, including multisite PTT (MS-PTT) from head-leg and hand-leg measurements, and multiwavelength PTT (MW-PTT) from RGB signals at the neonatal head (Fig. 2). PAT, based on the time delay between the ECG R-peak and three PPG morphological features (peaks, feet, and maximum first derivative), was used as a benchmark. These features were independently evaluated for BP estimation using multivariate regression models. Combining MS-PTT and MW-PTT yielded the best results, achieving a mean absolute error  $\pm$  standard deviation (MAE  $\pm$  STD) of  $7.65 \pm 7.48$  mmHg for SBP,  $6.31 \pm 5.58$  mmHg for DBP, and  $7.29 \pm 7.29$  mmHg for MBP, based on MLR subject-dependent modeling. According to the standard of the british hypertension society (BHS) in BP grading, these results meet the requirements for Grade C. This study offers initial evidence supporting the camera as a feasible approach for estimating the BP of neonates based on MS-PTT and MW-PTT features. This article has the following key contributions.

- 1) The first proof-of-concept clinical study for camera-based neonatal BP monitoring in NICU.
- 2) Exploration of a hybrid approach utilizing MS-PTT and MW-PTT for camera-based contactless BP estimation.

The remainder of this article is structured as follows. Section II reviews existing research works on contactless BP monitoring. Section III details the clinical setup and video processing framework proposed in this study. Section IV discusses the results of camera-based PTT measurement and BP regression. Finally, the conclusions are drawn in Section V.

## II. RELATED WORKS

Recent years have witnessed a growing interest in developing cuffless and contactless methods for adult BP estimation (as shown in Table I). However, their applications in neonatal BP monitoring remain to be explored. This section reviews contactless techniques for adult BP estimation, with a focus on their potential to be adapted for neonatal BP estimation.

Camera-based BP monitoring includes MS-PTT and MW-PTT techniques. The MS-PTT method relies on the delay in pulse wave traversing from its source to a peripheral distal location. Shao et al. [37] measured the PTT difference between mouth and palm. Jeong and Finkelstein [21] captured the face and right-hand palm using a high-speed camera running at 420 frames per second (fps). The interperson coefficient of correlation between SBP and PTT was  $-0.80 \pm 0.12$ . Fan et al. [22] proposed a novel contactless framework to estimate BP based on PTT. The developed algorithm adaptively selected reliable local rPPG pairs. Furthermore, an adaptive Gaussian model is developed to refine the morphology of rPPG waveform to improve the PTT estimation.

The MW-PTT method focuses on a single site, as different wavelengths with different skin penetration depths measure blood perfusion at different skin layers (e.g., systemic circulation and micro-circulation) [20], [36]. The red-IR wavelength can reach the subcutaneous blood volume variations, while the green wavelength can probe dermal arterioles [38]. In this case, PTT is mainly measured from different skin layers instead of different spatial locations. As shown in Table I, Liu et al. [18] found that the correlation between SBP and IR-Blue MW-PTT ( $|r| = 0.52$ ) was comparable to the correlation between SBP and PAT ( $|r| = 0.59$ ). Slapničar et al. [19] showed good absolute Pearson's correlation coefficient between both MW-PTT and systolic BP ( $R = 0.61, p = 0.08$ ) as well as diastolic BP ( $R = 0.54, p = 0.05$ ). This further achieved an MAE of 3.59 and 2.63 mmHg for SBP and DBP using the Random Forest regressor (RFR), respectively. Huang et al. [20], [39] revealed that the MW-PTT obtained by Green-NIR has a higher correlation with BP, and the fitted model has an MAE of 5.78 mmHg for SBP and 6.67 mmHg for DBP.

Similar to the cuffless method, single-site rPPG morphology was studied to estimate BP. Luo et al. [23] captured videos using an iPhone and extracted rPPG from 17 RoIs on the forehead, nose, cheek, lip, chin, and philtrum. The features extracted from spatial-redundant rPPG signals were input into a multilayer perceptron machine learning algorithm for SBP and DBP estimation. Jain et al. [24] extracted 20 time and frequency features and employed a linear regression for BP regression. Liao et al. [25] used forehead-rPPG and neck-BCG jointly and found that the augmented index derived from diastolic part of the waveform has a better correlation with

TABLE I  
OVERVIEW OF MOST RELEVANT WORKS ON CUFFLESS AND CONTACTLESS BP ESTIMATION

Technique	Reference	Population	Features	Model
Cuffless	Obrist <i>et al.</i> [6]	114 adults during rest and stress	PAT between EKG R-peak and PPG P-peak	Linear regression with SBP and DBP
	Chen <i>et al.</i> [7]	20 patients during cardiovascular surgery	High-frequency component of PAT	Linear model with SBP
	Poon <i>et al.</i> [8]	85 subjects (39 hypertensives)	PAT between EKG R-peak and PPG a characteristic point	Physical model with SBP and DBP
	Gesche <i>et al.</i> [9]	63 volunteers	PAT and PWV	Empirical mathematical function with SBP
	Ding <i>et al.</i> [10]	27 healthy subjects	PAT and PPG intensity ratio (PIR)	Combined Physical model with SBP and DBP
	Kim <i>et al.</i> [11]	15 healthy volunteers	PTT between BCG I wave and PPG P-peak	Linear regression with SBP, DBP, and MBP
	Chen <i>et al.</i> [12]	Five healthy subjects	PTT between BCG J wave and PPG P-peak	Linear regression with SBP and DBP
	Oyamada <i>et al.</i> [13]	Four healthy male	PTT between the chest and the abdomen SCG	Linear regression with SBP, DBP, and MBP
	Golberg <i>et al.</i> [14]	11 healthy adults	PTT between the chest and the wrist SCG	Physical model SBP and DBP
	Liu <i>et al.</i> [15]	MIMIC II database	14 new second derivative PPG features	SVR with SBP and DBP
	Lin <i>et al.</i> [16]	22 subjects	PPG features and PAT	Linear regression model with SBP and DBP
	Wang <i>et al.</i> [17]	32 subjects (4 with slightly low BP)	31 PPG features	Error feedback incremental SVR model with SBP and DBP
	Liu <i>et al.</i> [18]	10 healthy adult subjects	IR-Blue MW-PTT	Linear regression with SBP
Contactless	Slapničar <i>et al.</i> [19]	9 subjects	Green and near-infrared MW-PTT	Random Forest regression model with SBP and DBP
	Huang <i>et al.</i> [20]	17 adult participants	Green and near-infrared MW-PTT	Linear least squares regression with SBP and DBP
	Jeong <i>et al.</i> [21]	7 subjects	PTT between palm and head rPPG	Linear regression with SBP
	Fan <i>et al.</i> [22]	6 subjects	PTT between face and palm sub-regions	Empirical nonlinear function with SBP and DBP
	Luo <i>et al.</i> [23]	2348 subjects	155 unique features	Multilayer perceptron machine learning with SBP, DBP, and PP
	Jain <i>et al.</i> [24]	45 subjects	20 face rPPG features	Linear regression with SBP and DBP
	Liao <i>et al.</i> [25]	16 subjects	Features of forehead-rPPG and neck-BCG	Linear regression with SBP and DBP

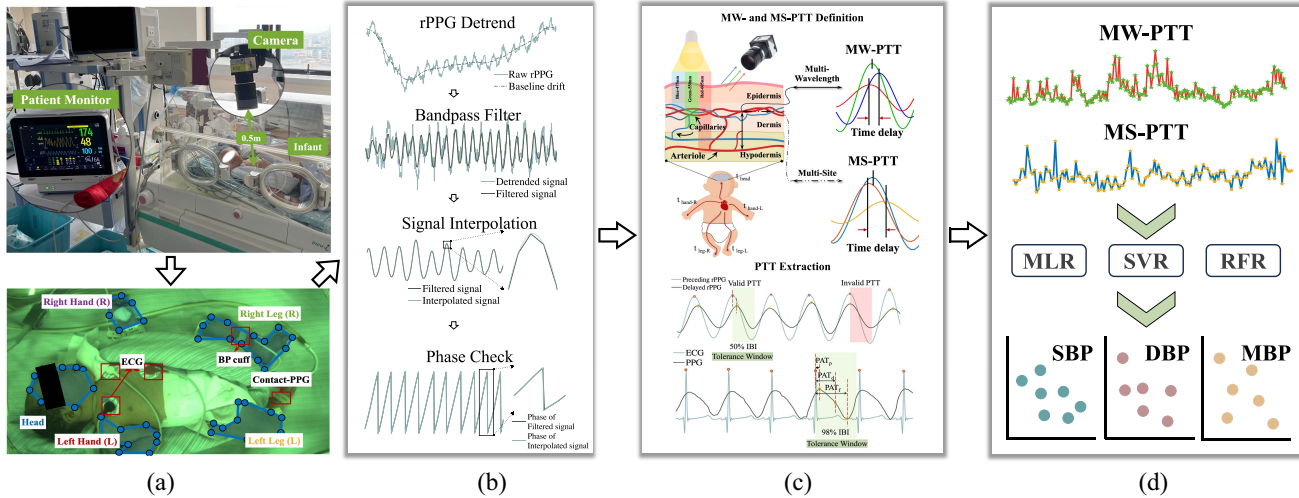


Fig. 2. Overview of the proposed BP estimation pipeline. The main steps include: (a) video capturing and body-RoI selection; (b) rPPG Extraction and Preprocessing; (c) rPPG from different body parts are used to extract MS-PTT, and optical signals with different wavelengths are measured to extract MW-PTT (MW-PTT: the rPPG waveforms from the RGB channels are color-coded to associate with their respective RGB channels; MS-PTT: blue - head rPPG, red - hand rPPG, yellow - foot rPPG.); (d) BP regression based on MW- and MS-PTT features.

DBP while the PTT (neck-forehead) is better correlated with SBP.

Although cuffless and contactless BP monitoring methods have been extensively studied among adults, they have not been validated for neonates. Neonates have significantly lower BP than adults, and the relationship between neonatal BP and PTT has yet to be studied. The key differences between neonates and adults are shown in Table II. Neonatal arteries are more elastic, and the arterial length difference is shorter, e.g., between the digital artery (hand) and the pedal artery (foot). The MS-PTT in neonates might be shorter compared to adults. The thinner skin of newborns, with an average thickness of about 1.0 mm compared to 2.5 mm in adults (as shown in Table II), allows more ambient light to pass through. Thus, the time delay between rPPG signals measured at different wavelengths might be reduced. MW-PTT between the rPPG signals from *G* and *R* channels will be less for thinner infant skin. Furthermore, The cardio-respiratory system of neonates is undeveloped and immature compared to adults,

TABLE II  
KEY DIFFERENCES BETWEEN NEONATES AND ADULTS

Aspect	Neonates	Adults
Skin thickness	0.9 - 1.2 mm	2.0 - 3.0 mm
Heart rate	120 - 160 bpm	60 - 100 bpm
Respiratory rate	30 - 60 bpm	10 - 20 bpm
SBP	60 - 90 mmHg	90 - 120 bpm
DBP	30 - 60 mmHg	60 - 80 bpm
Cardiovascular system	Unstable	Stable
Motion Artifacts	Involuntary movements	Still
Key Findings	Combination of MS-PTT and MW-PTT improves performance (Grade C in BHS)	Higher accuracy (e.g., Grade A/B in BHS)

thus the skin pulsatility is much weaker. Neonates can be more prone to involuntary body movement, which can interfere with the PTT measurement. This study aims to investigate the relationship between PAT/PTT and BP and to predict SBP, DBP, and MBP using MS-PTT, MW-PTT, as well as their combinations.

### III. MATERIALS AND METHODS

This study explores the feasibility of utilizing multiple PTT parameters extracted from video data for neonatal BP estimation. These parameters include MS-PTT, derived from various body regions, and MW-PTT, obtained from different skin layers. This section begins by detailing the clinical setup and experimental protocol employed in the study. Subsequently, we describe the rPPG extraction and preprocessing methods. Finally, the principles underlying PTT-based and PAT-based BP estimation are explained.

#### A. Clinical Setup and Data Collection

This study (IRB no.: NFEC-2022-100) was approved by the Institutional Review Board of Nanfang Hospital of Southern Medical University (Guangzhou, China). Written informed consent was obtained from the legal guardian of each neonate.

*1) Apparatus:* During data acquisition, a camera (IDS UI-3860CP-C-HQ) with an IMX290LQR-C CMOS sensor was mounted above the incubator, as shown in Fig. 2(a). The camera captured uncompressed raw videos of the neonates' whole body at a resolution of  $484 \times 274$  pixels and a frame rate of 60 fps, which is sufficient for PTT quantification [38], [39]. To maintain the quality of the rPPG signals, the white balance and autofocus functions were disabled throughout the recording process. Reference vital signs for each neonate were collected using a BeneVision M12 patient monitor (Mindray, China). This monitor recorded 3-lead ECG signals at 500 Hz and contact-PPG signals from the neonate's sole at 60 Hz. Cuff-based BP measurements were obtained every 3 min using a cuff placed on the neonate's arm or leg.

For the camera device, timestamps were recorded using the computer's internal clock, which was synchronized to the standard Beijing Time. All reference signals (i.e., ECG, contact-PPG, and cuff-based BP) were recorded with a shared timestamp synchronized to the standard Beijing Time, ensuring precise temporal alignment across modalities. This ensured that both devices were exactly aligned to the same reference time.

*2) Population:* A total of 40 neonates (28 males and 12 females) participated in this study. The participants included neonates with an average gestational age of 35.3 weeks ( $\pm 3.2$  weeks) and a postmenstrual age of 36.7 weeks ( $\pm 2.1$  weeks). The distributions of SBP, DBP, and MBP are visualized in Fig. 3. Quantitatively, the BP distributions of our dataset are  $68 \pm 10.72$  mmHg for SBP,  $38 \pm 8.27$  mmHg for DBP, and  $46 \pm 9.40$  mmHg for MBP (median  $\pm$  standard deviation), which are much lower than the adult's BP ranges. The study cohort consisted of neonates who met the following inclusion criteria: preterm birth (gestational age between 28 and 37 weeks), critical medical conditions (respiratory distress syndrome, hypoxic-ischemic encephalopathy, infection, or jaundice). Neonates requiring emergency first aid or diagnosed with infectious diseases were excluded from the study. Notably, no modifications were made to the standard monitoring and care routines of the neonates during the data collection process.

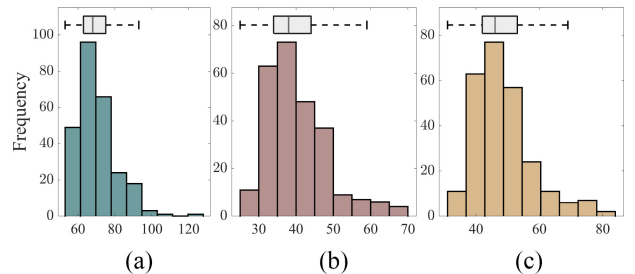


Fig. 3. Histogram and boxplots show the distribution of SBP, DBP, and MBP measured from neonates in our created clinical dataset.

*3) Experimental Protocol:* The experiment was conducted inside incubators under controlled environmental conditions. To ensure adequate illumination for video recording, an indoor fluorescent ceiling light was turned on throughout the study. The incubators maintained a stable temperature range of  $24^{\circ}\text{C}$ – $26^{\circ}\text{C}$  and a humidity range of 55%–65% to optimize neonatal comfort. BP measurements and video recordings were conducted during the neonates' sleep state. If a neonate woke up or cried, the experiment was paused until they returned to a calm sleep. This is to guarantee that the data are recorded at the quiet state of neonates in order to conclude the feasibility study. Notably, slight unintentional body movement during sleep did not disrupt the data collection process. The study protocol employed a cyclical mode consisting of three alternating phases: 1) resting phase (2.5 min); 2) BP measurement phase (0.5 min); and 3) resting phase (2.5 min). This cycle repeated 3–10 rounds for each neonate, resulting in a total of 258 valid BP data points. Video recordings of each neonate lasted between 10 and 30 min. The BP monitor (Mindray, China) was set to measure BP at 3-min intervals, with each BP measurement lasting approximately 0.5 min. This automated setup ensured accurate timing and consistent transitions between the phases.

#### B. rPPG Extraction and Preprocessing

Peripheral arteries were compressed during BP measurement, making pulse signals unavailable at that moment. We assume that the BP does not change significantly in a short period of time (e.g., 1 min). Therefore, we used the 30-s video clip that was one minute before the BP measurement for rPPG extraction and PTT analysis.

The rPPG signals were extracted based on a video processing framework detailed in Fig. 2. We used manual selection of skin region of interest (RoI) that ensures the accuracy of all RoI segmentation to conclude the feasibility study. The neonates remained stable and quiet in these 30 s. To avoid the instability caused by visual tracking (e.g. jitters), the five neonatal body regions were manually selected to extract the rPPG signal, including head, right hand, left hand, right leg, and left leg [as shown in Fig. 2(a)]. The raw rPPG signal (e.g., R, G, and B channels) was obtained by averaging the color intensity values within the defined RoI for each video frame. First, the baseline drift was removed from raw rPPG signals to eliminate low-frequency noise. Subsequently, a 4th-order bandpass filter was applied with a frequency range of

[1, 4] Hz to isolate the relevant components of the signal. The filtered signal was then interpolated to a sampling rate of 300 Hz to enhance the temporal resolution. Following the interpolation, we performed an instantaneous phase check on the interpolated signal to ensure its quality and consistency. The entire workflow is illustrated in Fig. 2(b).

For MS-PTT, the selected ROI combinations include four pairs: 1) Head–Right Leg; 2) Head–Left Leg; 3) Right Hand–Right Leg; and 4) Left Hand–Left Leg. For MW-PTT, the ROI is selected from the head region.

### C. Pulse Transit Time

PTT is the time interval for a pulse wave to travel between two peripheral skin sites [40]. Prior research has estimated BP using PAT that incorporates the preejection period (PEP) and PTT [41]. PAT is different from PTT, which focuses solely on the traveling time of pressure wave in the artery. PEP represents the time interval between the electrical depolarization of the heart, indicated by the QRS complex of an ECG, and the subsequent mechanical ventricular contraction that initiates blood ejection [42]. Therefore, PEP reflects the combined duration of electrical and mechanical events in the heart that precede blood ejection.

$$\text{PTT} = \text{PAT} - \text{PEP}. \quad (1)$$

While some studies have shown a correlation between BP and PAT (including the PEP) [9], [43], others have found that BP correlates better with PTT than PAT [42], [44], [45], because BP reflects the arterial properties (e.g., vessel stiffness), not a delay of actual ejection [46]. To this end, we benchmarked the camera-PTT based BP estimation with contact-PAT based BP estimation that is derived between ECG and PPG.

1) *Multisite Pulse Transit Time*: In this study, MS-PTT was calculated from four pairs of rPPG signals: 1) head-leg (left); 2) head-leg (right); 3) hand-leg (right); and 4) hand-leg (left). To ensure accurate MS-PTT calculation, we first validated the ROIs (i.e., those containing corresponding skin) from the specified combinations [head/hand-leg (right/left)]. Subsequently, the local neighborhood comparison method was used to detect peaks in the rPPG signal, which were further refined by setting parameters, such as a minimum peak distance of 0.25 s in this study. The time delay between two sets of peak locations was calculated to determine the MS-PTT. This value reflects the time difference between the pulse wave transmission to the two measured skin areas. The pulse typically reaches the head and hands slightly prior to the legs due to the anatomical distance from the heart. To ensure reliable PTT estimation, the following criteria were applied to check the validity of detected rPPG systolic peaks [see Fig. 2(c)].

- 1) *Peak Uniqueness*: There is only one systolic peak to be detected in one cardiac cycle. Any cardiac cycle with multiple peaks caused by motion noise will be excluded.
- 2) *Pulse Arrival Order*: The systolic peak in one cardiac cycle should appear earlier in the rPPG signal measured from the head or hand than that from the leg.
- 3) *Physiological Plausibility*: The calculated PTT should be less than half of the instantaneous HR derived from

the rPPG signals. Neonatal HR can range from 90 to 240 bpm (i.e., 0.25–0.5 s per beat). A newborn's height is approximately 0.5 m, and the distances between the heart and the head, hand, and leg are about 0.1, 0.2, and 0.4 m, respectively. With an arterial PWV of around 4 m/s [47], the MS-PTT for the head-leg (0.3 m) and hand-leg (0.2 m) is approximately 0.075 and 0.05 s.

Any PTT values that violated these criteria were assigned a *NaN* value. Afterward, we obtained a set of PTTs in 30-s rPPG pairs. A minimum number of valid PTT values were required for reliable estimation. This threshold was set to one-third of the total number of cardiac cycles within a 30-s window. Finally, the overall PTT for the 30-s recording was computed by averaging the set of valid PTT values that met the established criteria.

2) *Multiwavelength Pulse Transit Time*: Skin is a layered structure containing various blood vessels at different depths [see Fig. 2(c)]. Capillaries reside beneath the outermost epidermis layer. Arteries lie deep within the hypodermis. Branches of these arteries, known as arterioles, form a network of deep and superficial plexuses within the dermis. Since light penetration depth varies across different wavelengths, MW signals can capture blood volume changes in different skin layers. Blue and green wavelengths have shallower penetration depths (e.g., 0.5–1.0 mm) within the skin, making them primarily sensitive to blood volume changes in the capillary beds located near the dermis. Conversely, red and infrared (IR) light penetrates the small arteries within the hypodermis (e.g., 1.0–3.0 mm). Therefore, we can leverage different wavelengths to probe blood pulsation information in different types of arterial vessels [38].

Cardiac contraction generates a pulse wave that travels through the arterial network. The time delay between green-blue, red-green, and red-blue rPPG signals reflects the pulse wave propagation time from arterioles to capillaries in the skin. Therefore, the time delay measured between different MW rPPG signals holds promise for estimating arterial wall characteristics (i.e., vessel stiffness), which has shown to be negatively correlated with BP [18].

The MW-PTT calculation criteria for this step are identical to MS-PTT (Section III-C). Furthermore, the Pearson correlation coefficient (PCC) (*R*-value) is applied to measure the linear relationship between PTT/PAT and BP to assess the feasibility of camera-based neonatal BP measurement. Values closer to  $-1$  indicate a stronger negative correlation, which is to be expected. Additionally, a statistically significant correlation is confirmed by a *p*-value less than 0.05.

### D. Model Construction and Validation

Since the input features for BP regression have low dimensionality (i.e., maximally four elements), we only consider simple regression models with good interpretability and simplicity rather than deep learning models. Three multivariate analysis methods, namely, multivariate linear regression (MLR), support vector regression (SVR), and random forest regression (RFR) were adopted to construct the BP model based on the extracted PTT features.

For the subject-dependent model, the first 80% of each subject's data (in chronological order) is used as the training set, and the remaining 20% is reserved for testing. Additionally, we employ a fivefold cross-validation strategy on the 80% training data to perform parameter selection and optimize the model before final testing on the 20% test data. It is important to note that this Subject-dependent model is different from a fully personalized model (i.e., training the model based on the data from a single person). While the personalized model might be an option for model/device personalization, in reality, it is challenging to implement as each newly arrived infant would require a personalized calibration. Therefore, we consider a cross-subject (i.e., the training sets of all infants are combined for model training) approach to ensure better generalization and practical applicability.

For the subject-independent model, we adopted a leave-one-subject-out (LOSO) cross-validation strategy. Specifically, data from one subject is entirely excluded from the training process and used for testing, while the data from the remaining subjects is used for training. The final results are reported based on the performance of the test set (i.e., the excluded subject).

1) *MLR*: As the most widely used regression method, MLR models the relationship between a response variable and explanatory variables by fitting a linear formula. In our study, BP is the response variable, and PTT is the independent variable. The relationship between BP and the features can be expressed as follows:

$$BP = b_0 + \sum_{i=0}^n b_i PTT_i \quad (2)$$

where  $b_0$  is the intercept,  $n$  represents the number of PTT features (e.g., four types of MS-PTT, three types of MW-PTT, and MS-PTT+MW-PTT),  $b_i$  denotes the  $i$ th regression coefficient, and  $PTT_i$  denotes one of the PTT features. The coefficients were directly determined by minimizing the mean squared error (MSE) between the predicted and actual BP values.

2) *SVR*: SVR is a supervised learning algorithm specifically designed for regression tasks. In our implementation, we employed the radial basis function (RBF) kernel. The RBF kernel's hyperparameter gamma plays a crucial role in determining the influence radius of each training example, thereby controlling the model's ability to capture local patterns in the feature space. Two additional critical hyperparameters, C and Epsilon, govern the main optimization objective function of SVR. The parameter C controls the tradeoff between model complexity and training error tolerance, while Epsilon defines the width of the insensitive zone in the loss function. To achieve optimal model performance, we utilized grid search methodology for hyperparameter tuning (as shown in Table III). The basic formula of the SVR model can be expressed as

$$BP = \sum_{i=1}^n (\alpha_i - \alpha_i^*) K(PTT_i, PTT) + b \quad (3)$$

TABLE III  
SUMMARY OF HYPERPARAMETERS USED BY MACHINE LEARNING MODELS

Model	Hyperparameters
MLR	Fit intercept ∈ [True, False]
SVR	Kernel = 'rbf'
	Regularization parameter (C) ∈ [0.1, 1, <b>10</b> , 100]
	Kernel coefficient (gamma) ∈ ['scale', 'auto'] Epsilon ∈ [0.1, <b>0.5</b> ]
RFR	Number of estimators ∈ [5, 10, 50, <b>100</b> , 200]
	Quality of a split (criterion) ∈ ['MSE', 'MAE']
	Max depth = 15

Final selection of parameters is marked in **bold**.

where  $a_i$ ,  $\alpha_i^*$  denotes Lagrange multipliers,  $K(PTT_i, PTT)$  is the RBF kernel function,  $PTT_i$  is the  $i$ th feature vector of the training set, and  $b$  is the bias term.

3) *RFR*: RFR constructs a multitude of decision trees during training and outputs the average of predictions from all the individual trees. The hyperparameters were optimized using a grid search approach (as shown in Table III), and the final models were calibrated using all training data and the best estimator. RFR operates through the following steps.

- 1) *Bootstrap Sampling*: Random samples are drawn with replacements from the original training dataset. For each tree in the forest, a unique bootstrap sample is used.
- 2) *Tree Construction*: When growing individual trees, at each node, only a random subset of features is considered for splitting. The best split is determined based on the selected criterion (such as MSE or MAE). This process continues recursively until the tree reaches its stopping conditions, such as maximum depth.
- 3) *Prediction*: For making predictions, the random forest averages the predictions from all individual trees to produce the final output.

4) *Evaluation Metrics*: We evaluate the PCC and  $MAE \pm STD$  (MAPE%) between camera-based BP and reference BP. Additionally, the BHS standard is also used to assess the performance.

- 1) *PCC (R-value)*: This metric measures the linear relationship between camera-based BP and reference BP. Values closer to 1 indicate a stronger positive correlation. Additionally, a statistically significant correlation is confirmed by a p-value less than 0.05.
- 2) *MAE ± STD (MAPE%)*: This metric calculates the average and standard deviation of the absolute difference between the camera-based BP values and the reference BP measurements, and their corresponding percentage refer to mean absolute percentage error (MAPE). Lower MAE and STD values indicate better performance between the estimated and reference BP values.
- 3) *BHS Standard*: The BHS standard evaluates BP estimation methods based on the percentage of predictions falling within certain error ranges, assigning grades (A, B, or C) based on these percentages.

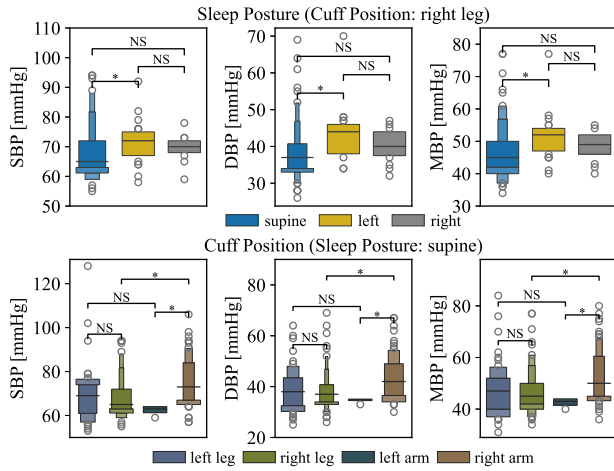


Fig. 4. Letter-value plots of SBP/DBP/MBP measurements during each neonatal sleep posture and cuff position. In letter-value plots, each progressively smaller pair of boxes around the center value (median) represents a power of two smaller fractions of the data points, such as fourths, eighths, sixteenths, and so on. The width of each small box represents the density of data points in that box. Kruskal-Wallis tests between each stimulus (NS: not significant, \*:  $p < 0.05$ ).

TABLE IV  
PEARSON'S CORRELATION COEFFICIENT BETWEEN BP AND MEAN PTT  
AT EACH BP LEVEL

	SBP R-value (p)	DBP R-value (p)	MBP R-value (p)
MS-PTT	<b>-0.39 (0.01)</b>	-0.15 (0.36)	<b>-0.44 (0.00)</b>
	<b>-0.58 (0.00)</b>	<b>-0.35 (0.03)</b>	<b>-0.62 (0.00)</b>
	-0.18 (0.25)	-0.08 (0.62)	<b>-0.34 (0.03)</b>
	<b>-0.64 (0.00)</b>	-0.27 (0.10)	<b>-0.58 (0.00)</b>
MW-PTT	<b>-0.53 (0.00)</b>	-0.19 (0.25)	<b>-0.42 (0.01)</b>
	<b>-0.56 (0.00)</b>	<b>-0.41 (0.01)</b>	<b>-0.57 (0.00)</b>
	<b>-0.63 (0.00)</b>	<b>-0.43 (0.01)</b>	<b>-0.52 (0.00)</b>
PAT	-0.21 (0.16)	-0.06 (0.72)	-0.14 (0.37)
	<b>-0.55 (0.00)</b>	<b>-0.58 (0.00)</b>	<b>-0.58 (0.00)</b>
	-0.16 (0.29)	-0.17 (0.29)	-0.23 (0.14)

**Boldface** denotes the entries with statistical significance ( $p < 0.05$ ).



Fig. 5. Snapshots from the videos used in the study, showing supine, left lateral, and right lateral sleep postures.

#### IV. RESULTS AND DISCUSSION

In this section, we first analyze the influence of sleep posture and cuff position on BP measurements, then a detailed analysis of the correlation between MS-PTT/MW-PTT and BP, followed by an evaluation of the BP estimation performance.

##### A. Impact of Sleep Posture and Cuff Position

The distributions of BP for each sleep state are shown in the first line of Fig. 4 via letter-value boxplots. The width of each small box indicates the density of data points. The cuff position is only chosen on the right leg for controlling variables. Since the neonatal arm is too small for wearing the cuff, most of the

BP measurements in our study were conducted on the neonatal leg.

The study was organized on infants in natural sleep postures without any intervention. The supine posture was predominant in the dataset as it is the most common sleep posture for newborns. In addition to supine, our dataset also include other postures (see Fig. 5), such as left lateral, and right lateral. The nonparametric Kruskal-Wallis test is used to determine whether there are statistically significant differences between the medians of three or more independent groups. Only a statistically significant difference exists between supine and left lateral BP measurements in neonates. SBP and DBP in the right lateral position did not show a statistically significant difference from those in the supine position. This is likely due to two factors: 1) the cuff is positioned below the level of the heart in the right lateral position, which tends to increase the BP and 2) the cuff is compressed in the right lateral position, which tends to affect the BP [48].

The distributions of BP for each cuff position are shown in the second line of Fig. 4 via letter-value boxplots. The sleep posture is only chosen on the supine for controlling variables. The Kruskal-Wallis test was used to examine the significance of ipsilateral limb (i.e., right arm and right leg), bilateral arm, and bilateral leg BP measurements. There is a statistically significant difference in BP measurements when the cuff was worn between right leg and right arm, and between left arm and right arm [4]. Furthermore, it is recommended to document the measurement site to ensure proper comparison and monitoring over time.

In actual NICU scenarios, the choice of BP measurement location is often constrained by various clinical factors, such as ongoing medical interventions (e.g., intravenous therapy, medication administration), and tissue compression effects from prolonged cuff placement. These factors sometimes necessitate alternating measurement sites to prevent tissue damage and ensure accurate readings. This situation particularly highlights the advantages of our camera-based approach, as it offers a noncontact measurement solution that eliminates concerns about tissue compression and physical constraints associated with traditional cuff measurements. Furthermore, a key advantage of the camera-based system enables simultaneous monitoring of multiple body regions. This capability allows for greater flexibility in real-time selection of the optimal ROI, in contrast to contact sensors, which can only measure the signal from that specific part.

##### B. Feasibility of Camera-PTT for BP Calibration

The measurable ranges of both PTT types are compared to understand their reliability in infants. The ranges for MS-PTT are estimated as follows: head-leg (right):  $25.0 \pm 11.3$  ms, head-leg (left):  $24.0 \pm 11.5$  ms, hand-leg (right):  $28.7 \pm 12.7$  ms, and hand-leg (left):  $28.2 \pm 14.2$  ms. For MW-PTT, the ranges are: green-blue:  $15.1 \pm 8.2$  ms, red-green:  $14.6 \pm 8.1$  ms, and red-blue:  $20.9 \pm 10.9$  ms. MS-PTT shows the systemic peripheral arterial PWV. MW-PTT reflects the PWV at the micro-circulation level, which is closely

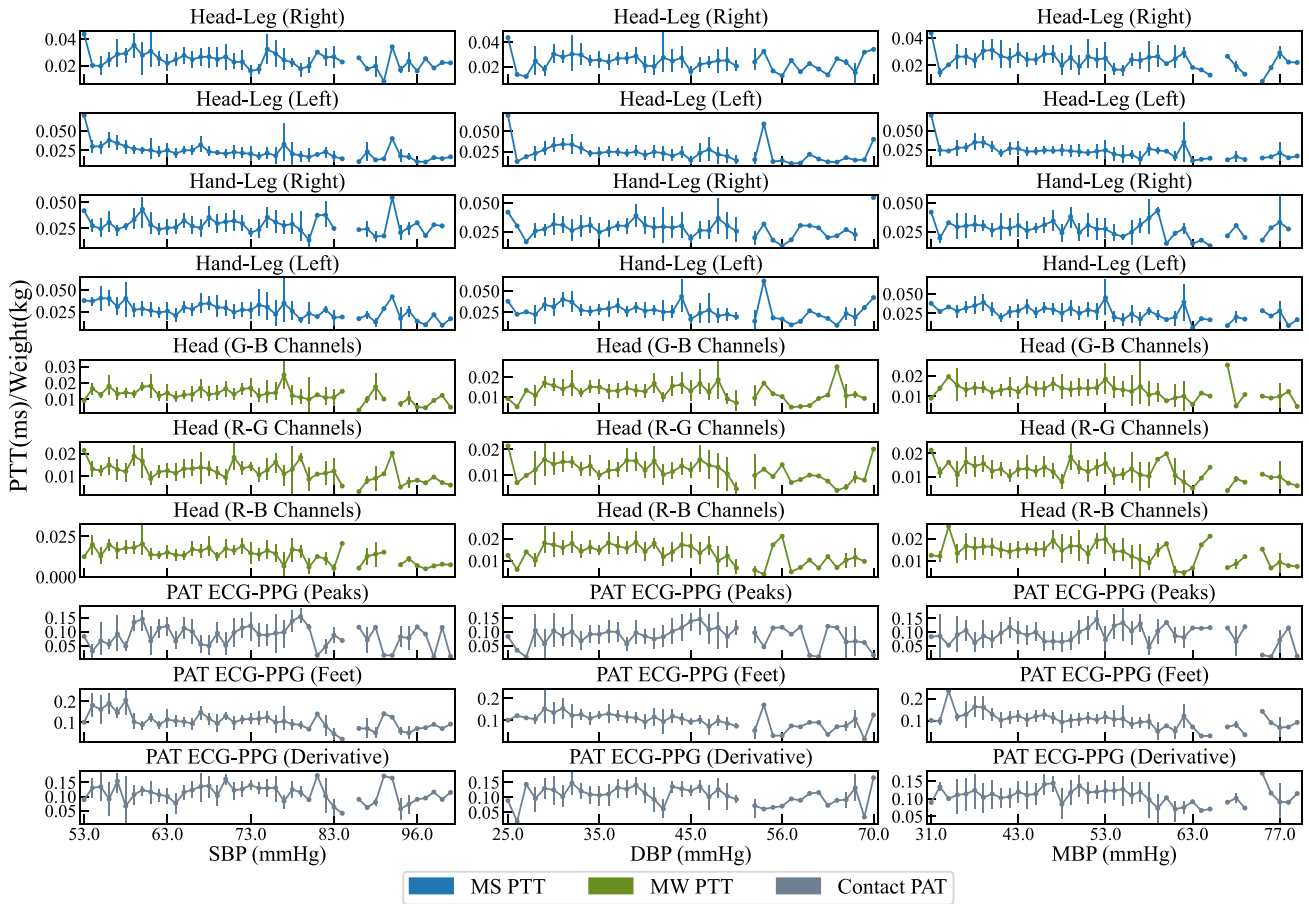


Fig. 6. Errorbars visualize the relationship between BP (SBP/DBP/MBP) and normalized PTT/PAT. Blue errorbars represent MS-PTT with four combinations: Head-Leg (Left/Right) and Hand-Leg (Left/Right). Green errorbars depict MW-PTT with three combinations: Green-Blue, Red-Green, and Red-Blue channels. Gray errorbars represent ECG-PPG-based PAT calculated from ECG R-peaks and contact-PPG features (peaks, feet, or maximum first derivative).

associated with the capillary resistance and elastic properties of the skin vasculature.

We used the neonatal weight obtained on the recording day to normalize MS- and MW-PTT measurements to minimize variations between individuals. While height is commonly used to normalize PTT, it is not measured in the clinical routine on daily-basis for neonates, making weight a more practical and accessible metric. Additionally, weight can also be approximately estimated using a single image [49], further supporting its feasibility in clinical settings. The normalization of MS- and MW-PTT by weight helps to account for interindividual differences in body size and composition, which influence the speed of pulse wave propagation. Infants with larger body size typically have longer PTT due to increased vascular length, with smaller body size the shorter PTT.

1) **MS-PTT:** For infants, the PTT (PPG time delay) between infants' hand and foot differs from adults due to the lower BP range, smaller body size, and greater vascular elasticity, higher HR. We can assume that the length difference from hand to foot is shorter, approximately 0.2 m (compared to 0.75 m in adults). Due to softer and more elastic blood vessels, PWV in infants is lower, around 3.6 m/s [47] (compared to 5 m/s in adults). Thus, infant's PPG time difference between hand and foot is approximately 55 ms. In addition to

the camera-based experiment, we did an experiment using two contact-based PPG sensors, focusing on a more deterministic proof-of-concept study of MS-PTT in BP calibration (see the Appendix).

One to four rows of Fig. 6 show the distribution between BP and camera-based MS-PTT (blue errorbars). We assessed the correlation between mean MS-PTT at each BP level (SBP, DBP, and MBP) using Pearson's correlation coefficient (shown in Table IV). The results demonstrated that most mean MS-PTT values exhibited a statistically significant negative correlation with BP, while only a small proportion of MS-PTT values showed no statistical significance. The correlations ( $R$ -value) are  $-0.64$  between SBP and mean MS-PTT [Hand-Leg (left)] at each BP level, and  $-0.62$  between MBP and mean MS-PTT [Head-Leg (left)] at each BP level. This observation aligns with earlier findings on the relationship between BP and PTT [22].

2) **MW-PTT:** The thinner skin of newborns, with an average thickness of about 1.0 mm compared to 2.5 mm in adults, allows more ambient light to pass through. Thus, the time delay between rPPG signals obtained at different wavelengths might be reduced. MW-PTT between the rPPG signals from G and R channels will be less for thinner infant skin. Based on our camera-based MW-PTT results in neonates, the ranges are: green-blue:  $15.1 \pm 8.2$  ms, red-green:  $14.6 \pm 8.1$  ms, and

TABLE V  
MAE  $\pm$  STD (MAPE%) OF UNIVARIATE SETTING FOR BP REGRESSION

Subject-Dependent	SBP (mmHg)			DBP (mmHg)			MBP (mmHg)			
	MLR	SVR	RFR	MLR	SVR	RFR	MLR	SVR	RFR	
MS-PTT	Head-Leg (Right)	8.57 $\pm$ 10.17(11.40%)	8.68 $\pm$ 10.37(11.43%)	10.44 $\pm$ 10.25(14.16%)	6.83 $\pm$ 5.84(17.26%)	6.66 $\pm$ 5.76(16.69%)	8.33 $\pm$ 6.60(21.14%)	7.76 $\pm$ 7.86(15.40%)	7.52 $\pm$ 8.06(14.63%)	9.64 $\pm$ 8.29(19.43%)
	Head-Leg (Left)	8.32 $\pm$ 9.60(11.06%)	8.51 $\pm$ 9.87(11.16%)	<b>7.90 <math>\pm</math> 10.02(10.39%)</b>	6.49 $\pm$ 5.55(16.39%)	6.30 $\pm$ 6.31(15.55%)	6.70 $\pm$ 6.46(16.61%)	<b>7.39 <math>\pm</math> 7.50(14.67%)</b>	7.37 $\pm$ 7.91(14.35%)	7.42 $\pm$ 7.97(14.45%)
	Hand-Leg (Right)	<b>8.21 <math>\pm</math> 7.90(11.29%)</b>	8.41 $\pm$ 8.24(11.42%)	9.41 $\pm$ 9.54(12.89%)	6.75 $\pm$ 6.69(17.01%)	6.62 $\pm$ 6.26(16.24%)	7.23 $\pm$ 7.20(18.14%)	7.68 $\pm$ 7.38(15.27%)	7.65 $\pm$ 7.93(14.92%)	8.46 $\pm$ 8.73(16.77%)
	Hand-Leg (Left)	8.75 $\pm$ 9.75(11.70%)	8.70 $\pm$ 10.24(11.39%)	9.39 $\pm$ 8.89(13.00%)	6.79 $\pm$ 5.64(17.25%)	6.41 $\pm$ 5.88(15.79%)	6.83 $\pm$ 5.25(18.14%)	7.76 $\pm$ 7.59(15.48%)	7.39 $\pm$ 7.88(14.38%)	7.88 $\pm$ 6.66(16.50%)
MW-PTT	Green-Blue	8.87 $\pm$ 9.58(11.95%)	8.48 $\pm$ 9.15(11.35%)	9.63 $\pm$ 8.20(13.44%)	6.99 $\pm$ 5.54(17.81%)	6.65 $\pm$ 5.55(16.87%)	7.11 $\pm$ 5.98(18.87%)	8.02 $\pm$ 7.35(16.12%)	7.45 $\pm$ 7.25(14.91%)	8.21 $\pm$ 7.09(17.15%)
	Red-Green	9.03 $\pm$ 9.70(12.17%)	8.61 $\pm$ 9.79(11.41%)	10.28 $\pm$ 11.03(13.59%)	6.89 $\pm$ 5.75(17.49%)	6.56 $\pm$ 6.09(16.42%)	6.89 $\pm$ 7.04(16.70%)	7.97 $\pm$ 7.58(15.95%)	7.55 $\pm$ 8.01(14.75%)	8.35 $\pm$ 9.06(16.12%)
	Red-Blue	8.96 $\pm$ 9.53(12.09%)	8.67 $\pm$ 9.32(11.61%)	9.40 $\pm$ 9.99(12.80%)	6.93 $\pm$ 5.68(17.64%)	6.28 $\pm$ 6.04(15.66%)	7.26 $\pm$ 6.77(18.60%)	7.98 $\pm$ 7.47(16.01%)	7.35 $\pm$ 7.56(14.50%)	8.19 $\pm$ 8.25(16.56%)
PAT	ECG-PPG (Peaks)	8.77 $\pm$ 9.97(11.73%)	8.31 $\pm$ 9.75(10.96%)	8.01 $\pm$ 10.42(10.58%)	6.85 $\pm$ 5.77(17.36%)	6.17 $\pm$ 5.85(15.32%)	<b>6.04 <math>\pm</math> 5.82(14.81%)</b>	7.90 $\pm$ 7.66(15.76%)	7.16 $\pm$ 7.67(13.97%)	<b>7.02 <math>\pm</math> 7.77(13.59%)</b>
	ECG-PPG (Feet)	8.82 $\pm$ 9.42(11.81%)	<b>8.30 <math>\pm</math> 9.73(10.96%)</b>	9.01 $\pm$ 9.89(12.01%)	<b>6.45 <math>\pm</math> 5.77(16.45%)</b>	<b>6.12 <math>\pm</math> 5.76(15.32%)</b>	6.83 $\pm$ 6.52(17.11%)	7.46 $\pm$ 7.59(14.91%)	7.25 $\pm$ 7.60(14.15%)	8.02 $\pm$ 8.32(15.88%)
	ECG-PPG (Deviation)	8.99 $\pm$ 9.97(12.09%)	8.55 $\pm$ 9.75(11.20%)	9.08 $\pm$ 9.60(12.20%)	6.88 $\pm$ 5.88(17.54%)	6.25 $\pm$ 5.57(15.72%)	6.78 $\pm$ 6.17(17.26%)	7.88 $\pm$ 7.77(15.79%)	<b>7.09 <math>\pm</math> 7.51(13.76%)</b>	7.68 $\pm$ 7.90(15.19%)
Subject-Independent	MLR	SVR	RFR	MLR	SVR	RFR	MLR	SVR	RFR	
MS-PTT	Head-Leg (Right)	<b>7.19 <math>\pm</math> 6.25(10.05%)</b>	7.42 $\pm$ 6.06(10.57%)	<b>7.26 <math>\pm</math> 6.56(10.31%)</b>	<b>5.74 <math>\pm</math> 5.01(14.18%)</b>	<b>5.93 <math>\pm</math> 5.17(14.78%)</b>	6.66 $\pm$ 6.00(16.74%)	<b>6.35 <math>\pm</math> 5.62(12.80%)</b>	6.71 $\pm$ 5.77(13.94%)	6.97 $\pm$ 6.36(14.40%)
	Head-Leg (Left)	9.53 $\pm$ 8.45(12.92%)	7.78 $\pm$ 6.29(11.17%)	8.83 $\pm$ 6.57(12.95%)	6.73 $\pm$ 6.31(15.70%)	7.97 $\pm$ 5.66(20.99%)	9.01 $\pm$ 6.31(24.09%)	7.68 $\pm$ 7.19(14.80%)	8.07 $\pm$ 6.07(17.25%)	9.38 $\pm$ 6.61(20.41%)
	Hand-Leg (Right)	7.20 $\pm$ 6.01(10.10%)	7.46 $\pm$ 6.08(10.47%)	8.19 $\pm$ 6.50(11.58%)	5.84 $\pm$ 5.09(14.22%)	6.09 $\pm$ 5.22(14.92%)	6.67 $\pm$ 5.36(16.80%)	6.41 $\pm$ 5.72(12.80%)	6.72 $\pm$ 5.65(13.61%)	7.41 $\pm$ 5.99(15.27%)
	Hand-Leg (Left)	9.33 $\pm$ 7.81(12.72%)	6.99 $\pm$ 7.09(9.71%)	7.75 $\pm$ 7.35(10.90%)	6.91 $\pm$ 6.39(16.18%)	6.18 $\pm$ 5.32(15.45%)	6.53 $\pm$ 5.55(16.24%)	7.81 $\pm$ 7.00(15.18%)	6.78 $\pm$ 5.89(13.92%)	7.01 $\pm$ 6.17(14.31%)
MW-PTT	Green-Blue	10.03 $\pm$ 7.65(14.04%)	7.48 $\pm$ 6.14(10.54%)	8.03 $\pm$ 6.79(11.15%)	6.71 $\pm$ 5.27(16.42%)	5.98 $\pm$ 5.18(14.83%)	<b>6.30 <math>\pm</math> 5.51(15.31%)</b>	7.86 $\pm$ 6.32(15.75%)	6.50 $\pm$ 5.79(13.12%)	<b>6.93 <math>\pm</math> 6.19(13.85%)</b>
	Red-Green	8.52 $\pm$ 7.01(11.92%)	7.27 $\pm$ 6.19(10.47%)	7.95 $\pm$ 6.60(11.45%)	6.36 $\pm$ 4.77(16.12%)	6.56 $\pm$ 4.83(17.05%)	6.38 $\pm$ 5.14(16.53%)	7.13 $\pm$ 5.58(14.63%)	6.88 $\pm$ 5.48(14.52%)	6.99 $\pm$ 5.86(14.78%)
	Red-Blue	9.80 $\pm$ 7.85(13.59%)	<b>6.90 <math>\pm</math> 6.39(9.82%)</b>	7.85 $\pm$ 6.52(11.31%)	6.63 $\pm$ 5.53(16.19%)	6.10 $\pm$ 4.89(15.58%)	6.86 $\pm$ 5.43(17.66%)	7.79 $\pm$ 6.62(15.50%)	<b>6.30 <math>\pm</math> 5.86(13.03%)</b>	7.21 $\pm$ 6.08(15.13%)
PAT	ECG-PPG (Peaks)	7.99 $\pm$ 6.11(11.39%)	8.28 $\pm$ 6.51(11.66%)	9.66 $\pm$ 7.71(13.68%)	6.39 $\pm$ 4.66(16.48%)	6.34 $\pm$ 5.25(15.66%)	7.62 $\pm$ 6.16(18.92%)	7.09 $\pm$ 5.31(14.79%)	7.16 $\pm$ 5.97(14.55%)	8.41 $\pm$ 6.98(17.20%)
	ECG-PPG (Feet)	10.64 $\pm$ 7.63(14.61%)	8.90 $\pm$ 6.98(12.34%)	10.28 $\pm$ 7.57(13.98%)	8.18 $\pm$ 6.11(19.43%)	6.68 $\pm$ 5.83(15.92%)	7.33 $\pm$ 6.20(17.05%)	8.93 $\pm$ 6.64(17.59%)	7.99 $\pm$ 6.70(15.71%)	8.14 $\pm$ 6.77(15.70%)
	ECG-PPG (Deviation)	7.56 $\pm$ 5.73(10.72%)	7.46 $\pm$ 6.10(10.35%)	8.19 $\pm$ 6.82(11.29%)	5.93 $\pm$ 5.08(14.59%)	6.18 $\pm$ 5.81(14.51%)	6.30 $\pm$ 5.89(15.08%)	6.58 $\pm$ 5.53(13.38%)	6.77 $\pm$ 6.09(13.21%)	7.07 $\pm$ 6.60(13.94%)

**Boldface** denotes the smallest MAE using different univariate features for BP regression.

red-blue:  $20.9 \pm 10.9$  ms, which is much lower than adults' MW-PTT (i.e., 46 ms [19]).

The green errorbars in Fig. 6 illustrate the distribution of MW-PTT values at each BP level. The correlations (*R*-value) between SBP and mean MW-PTT are  $-0.56$  for Red-Green channels, and  $-0.63$  for Red-Blue channels. Similarly, the correlations (*R*-value) between MBP and mean MW-PTT are  $-0.57$  for the Red-Green channels, and  $-0.52$  for Red-Blue channels. All MW-PTT measurements exhibited statistically significant correlations with both SBP and MBP. The combination of Red-Green and Red-Blue demonstrated statistically significant correlations with DBP, with *R*-values of  $-0.41$  and  $-0.43$ , respectively. Since MW-PTT only involves a single body part instead of multiple body parts like MS-PTT, MW-PTT is easier to measure. The previous research leveraged the NIR - Green channels to calculate MW-PTT using a narrow-band camera for adults' BP measurements [20], [36]. Infants have relatively shallow and dense subcutaneous blood vessels. The thinner neonatal epidermis and dermis, compared to adults, allow light to penetrate deeper into the hypodermis, where small arteries reside. This leads to a small delay between rPPG signals obtained at different wavelengths (e.g., red-green) because these wavelengths can reach similar skin layers in neonates. Similarly, the Blue wavelength can penetrate deeper than that of adults, allowing it to obtain a MW-PTT with the Red/Green wavelength from pulses in the epidermis and dermis. Overall, choosing the red wavelength in our study is more practical than the NIR wavelength because NIR requires additional lighting.

3) *Benchmark PAT (ECG-PPG)*: PAT measures the time delay between an *R*-peak of ECG and specific features (peak, foot, or maximum first derivative) of the corresponding contact-PPG signal. The gray errorbars in Fig. 6 show the distribution of PAT values at each BP level. When using peaks or maximum first derivative features of contact-PPG for PAT calculation, the relationship between mean PAT and BP is not statistically significant. The PAT from ECG and the feet of

contact-PPG show a downward trend with SBP/DBP/MBP (*R*-value:  $-0.55$ ,  $-0.58$ , and  $0.58$ , respectively). Notably, the foot of contact-PPG signal appears to be a more appropriate feature for PAT calculation. It exhibits a more pronounced decreasing trend with the increase of BP in Fig. 6 and its correlations with SBP, DBP, and MBP are stronger than other PAT features.

### C. Blood Pressure Estimation

To evaluate the effectiveness of each MS-PTT, MW-PTT, and PAT for BP estimation, we employed three machine-learning-based regression algorithms: 1) MLR; 2) SVR; and 3) RFR. We assessed the univariate performance of each method using the MAE  $\pm$  STD (MAPE%). The details can be referred to in Table V. Additionally, we explored the potential combination of these features, including four MS-PTT and three MW-PTT measurements, leading to a total of seven MS+MW-PTT measurements. ECG and PPG based PAT-BP regression have three measurements. The results of BP regression using these combined features are presented in Table VI (MAE  $\pm$  STD and PCC).

1) *Univariate for BP Regression*: A total of seven MS-PTTs, MW-PTTs, and three PATs are separately used for univariate BP estimation, as shown in Table V. The Head-Leg (Left) MS-PTT measurements achieve an MAE  $\pm$  STD of  $7.90 \pm 10.02$  for SBP regression in the subject-dependent RFR setting, while the Red-Green MW-PTT achieves an MAE  $\pm$  STD of  $6.90 \pm 6.39$  for SBP regression in the subject-independent SVR setting. For DBP regression, the ECG-PPG (Peaks) PAT yields an MAE  $\pm$  STD of  $6.04 \pm 5.82$  in the subject-dependent RFR setting, and the Head-Leg (Right) MS-PTT achieves an MAE  $\pm$  STD of  $5.74 \pm 5.01$  in the subject-independent MLR setting. Additionally, for MBP regression, the ECG-PPG (Peaks) PAT shows an MAE  $\pm$  STD of  $7.02 \pm 7.77$  in the subject-dependent RFR setting, while the Red-Green MW-PTT achieves an MAE  $\pm$  STD of  $6.30 \pm 5.86$  in the subject-independent SVR setting. Based on the above results, the ECG-PPG (Peaks) PAT in the subject-dependent

**TABLE VI**  
MAE  $\pm$  STD (MAPE%) AND PCC OF MULTIVARIATE SETTING FOR BP REGRESSION

MAE $\pm$ STD (MAPE%)		SBP (mmHg)			DBP (mmHg)			MBP (mmHg)		
Subject-Dependent		MLR	SVR	RFR	MLR	SVR	RFR	MLR	SVR	RFR
MS-PTT		7.89 $\pm$ 7.66(10.79%)	10.31 $\pm$ 7.94(14.43%)	8.80 $\pm$ 7.81(12.19%)	6.62 $\pm$ 5.48(16.58%)	8.03 $\pm$ 6.10(20.62%)	7.34 $\pm$ 5.72(18.69%)	7.55 $\pm$ 7.26(14.89%)	9.00 $\pm$ 7.58(18.22%)	8.34 $\pm$ 7.14(16.80%)
MW-PTT		8.77 $\pm$ 0.55(1.80%)	8.67 $\pm$ 0.31(11.61%)	8.77 $\pm$ 0.79(11.86%)	6.80 $\pm$ 5.58(17.30%)	6.45 $\pm$ 5.78(16.33%)	6.54 $\pm$ 5.28(16.67%)	7.82 $\pm$ 0.44(15.67%)	7.30 $\pm$ 0.43(14.48%)	7.57 $\pm$ 0.11(15.22%)
MS+MW-PTT		<b>7.65 <math>\pm</math> 7.48(10.45%)</b>	8.62 $\pm$ 6.47(11.90%)	8.48 $\pm$ 6.64(11.80%)	<b>6.31 <math>\pm</math> 5.58(15.65%)</b>	6.89 $\pm$ 4.95(17.65%)	6.90 $\pm$ 5.58(17.43%)	<b>7.29 <math>\pm</math> 7.29(14.30%)</b>	8.18 $\pm$ 6.02(16.57%)	8.04 $\pm$ 6.86(16.14%)
PAT		8.82 $\pm$ 0.24(11.90%)	<b>7.66 <math>\pm</math> 8.81(10.15%)</b>	<b>6.82 <math>\pm</math> 7.33(9.14%)</b>	6.68 $\pm$ 5.69(17.11%)	<b>6.31 <math>\pm</math> 5.01(16.01%)</b>	<b>5.17 <math>\pm</math> 4.76(13.34%)</b>	7.68 $\pm$ 7.48(15.48%)	<b>7.18 <math>\pm</math> 6.48(14.39%)</b>	<b>5.89 <math>\pm</math> 6.09(11.79%)</b>
Subject-Independent		MLR	SVR	RFR	MLR	SVR	RFR	MLR	SVR	RFR
MS-PTT		<b>7.13 <math>\pm</math> 6.07(10.25%)</b>	8.21 $\pm$ 6.75(11.69%)	7.89 $\pm$ 6.61(11.34%)	<b>5.92 <math>\pm</math> 5.20(15.05%)</b>	6.56 $\pm$ 5.69(16.48%)	<b>6.32 <math>\pm</math> 5.58(16.04%)</b>	<b>6.56 <math>\pm</math> 5.74(13.65%)</b>	<b>7.37 <math>\pm</math> 6.34(15.24%)</b>	<b>6.97 <math>\pm</math> 6.26(14.50%)</b>
MW-PTT		7.61 $\pm$ 5.94(11.07%)	8.24 $\pm$ 6.80(11.77%)	8.12 $\pm$ 6.41(11.82%)	6.22 $\pm$ 5.16(15.98%)	6.65 $\pm$ 6.42(16.58%)	6.63 $\pm$ 6.05(16.98%)	6.92 $\pm$ 5.70(14.56%)	7.52 $\pm$ 6.86(15.38%)	7.33 $\pm$ 6.50(15.40%)
MS+MW-PTT		7.29 $\pm$ 6.09(10.49%)	<b>8.10 <math>\pm</math> 7.09(11.52%)</b>	<b>7.89 <math>\pm</math> 5.98(11.42%)</b>	5.92 $\pm$ 5.32(15.01%)	<b>6.52 <math>\pm</math> 6.11(16.50%)</b>	6.40 $\pm$ 5.62(16.38%)	6.67 $\pm$ 5.85(13.85%)	7.39 $\pm$ 6.78(15.29%)	7.10 $\pm$ 6.04(14.89%)
PAT		7.58 $\pm$ 5.61(10.98%)	8.41 $\pm$ 6.74(12.06%)	8.66 $\pm$ 6.74(12.43%)	6.05 $\pm$ 4.96(15.51%)	6.74 $\pm$ 5.59(17.16%)	6.98 $\pm$ 5.78(17.55%)	6.73 $\pm$ 5.51(14.11%)	7.70 $\pm$ 6.43(16.02%)	7.64 $\pm$ 6.35(15.78%)
PCC		SBP (mmHg)			DBP (mmHg)			MBP (mmHg)		
Subject-Dependent		MLR	SVR	RFR	MLR	SVR	RFR	MLR	SVR	RFR
MS-PTT		0.37(0.01)*	0.01(0.97)	0.15(0.33)	0.37(0.01)*	0.03(0.84)	0.14(0.35)	0.32(0.03)*	0.09(0.53)	0.17(0.27)
MW-PTT		0.23(0.11)	0.31(0.03)*	0.37(0.01)*	0.18(0.20)	0.26(0.06)	0.35(0.01)*	0.19(0.20)	0.32(0.02)*	0.34(0.01)*
MS+MW-PTT		0.44(0.00)*	0.42(0.00)*	0.40(0.01)*	0.41(0.00)*	0.38(0.01)*	0.24(0.11)	0.37(0.01)*	0.39(0.01)*	0.28(0.06)
PAT		0.27(0.06)	0.54(0.00)*	0.70(0.00)*	0.23(0.11)	0.44(0.00)*	0.63(0.00)*	0.23(0.11)	0.49(0.00)*	0.66(0.00)*
Subject-Independent		MLR	SVR	RFR	MLR	SVR	RFR	MLR	SVR	RFR
MS-PTT		0.16(0.02)*	-0.04(0.59)	-0.02(0.77)	0.07(0.29)	0.02(0.77)	-0.01(0.89)	0.09(0.21)	-0.01(0.86)	-0.01(0.92)
MW-PTT		0.03(0.69)	-0.21(0.00)*	-0.02(0.76)	-0.18(0.01)*	-0.26(0.00)*	-0.22(0.00)*	-0.12(0.08)	-0.27(0.00)*	-0.16(0.02)*
MS+MW-PTT		0.15(0.02)*	-0.05(0.44)	0.04(0.58)	0.07(0.32)	-0.05(0.42)	-0.11(0.09)	0.06(0.37)	-0.09(0.17)	-0.07(0.32)
PAT		0.17(0.01)*	-0.10(0.16)	-0.10(0.14)	0.13(0.06)	-0.08(0.24)	-0.11(0.09)	0.12(0.07)	-0.14(0.04)*	-0.09(0.21)

- 1) **Boldface** represent the smallest MAE using different multivariate for BP regression.  
2) \* denotes the entries with statistical significance ( $p < 0.05$ ).

**TABLE VII**  
COMPARISON OF BP ESTIMATION RESULTS WITH BHS STANDARD

		Subject-dependent			Subject-independent					
Cumulative Error Percentage		$\leq 5$ mmHg	$\leq 10$ mmHg	$\leq 15$ mmHg	$\leq 5$ mmHg	$\leq 10$ mmHg	$\leq 15$ mmHg			
	BHS	A 0.60	0.85	0.95	0.60	0.85	0.95			
	B	0.50	0.75	0.90	0.50	0.75	0.90			
	C	0.40	0.65	0.85	0.40	0.65	0.85			
MS-PTT	MLR	SBP <b>0.41</b> DBP <b>0.50</b> MBP <b>0.46</b>	0.74 0.85 0.83	0.91 0.91 0.91	0.44 0.41 0.42	0.72 0.69 0.69	0.91 0.85 0.89			
	SVR	SBP 0.33	0.57	0.76	0.50	0.86	0.94			
	RF	SBP 0.41	0.65	0.87	0.47	0.83	0.94			
MW-PTT	MLR	SBP 0.40	0.70	0.90	0.37	0.74	0.88			
	SVR	SBP 0.32	0.72	0.90	0.47	0.84	0.95			
	RF	SBP 0.36	0.74	0.88	0.45	0.79	0.93			
MS+MW	MLR	SBP 0.48	0.86	0.92	0.37	0.69	0.89			
	SVR	SBP 0.32	0.72	0.90	0.48	0.80	0.92			
	RF	SBP 0.36	0.74	0.88	0.45	0.73	0.90			
PAT	MLR	SBP 0.48	0.76	0.89	0.44	0.72	0.91			
	SVR	SBP 0.41	0.83	0.91	0.51	0.79	0.92			
	RF	SBP 0.41	0.80	0.93	0.48	0.72	0.88			

The background colors in the table represent the levels of compliance with the BHS standards:

- 1) red indicates compliance with Grade C,
- 2) yellow indicates compliance with Grade B,
- 3) green indicates compliance with Grade A.

setting and the Red-Blue MW-PTT in the subject-independent setting demonstrate potential for BP regression. However, it remains challenging to determine which variable exhibits the best BP regression performance.

2) *Multivariate for BP Regression:* We investigated the performance of combining multiple features for BP regression.

The combined MS-PTT feature set included measurements from four channels: head/hand-leg (right) and head/hand-leg (left). The MW-PTT combination used the pairs of three RGB wavelengths. Finally, the multi-PAT combinations included PAT values derived from peak, foot, and the maximum first derivative of the contact-PPG waveform. Table VI presents the MAE  $\pm$  STD (MAPE%) and PCC for these multivariate BP regressions, and Table VII illustrates the BP regression results compared with BHS standard. Fig. 7 presents the correlation scatter plots and Bland-Altman plots for BP estimation using the MS+MW-PTT MLR model.

In the subject-dependent MLR setting, MS+MW-PTT achieves  $7.65 \pm 7.48$  for SBP regression,  $6.31 \pm 5.58$  for DBP regression, and  $7.29 \pm 7.29$  for MBP regression. The proposed framework (MS+MW-PTT, MLR model) achieves the following cumulative coverage rates according to BHS standard:  $\leq 5$  mmHg: 48%,  $\leq 10$  mmHg: 76%,  $\leq 15$  mmHg: 89% for SBP;  $\leq 5$  mmHg: 54%,  $\leq 10$  mmHg: 85%,  $\leq 15$  mmHg: 91% for DBP;  $\leq 5$  mmHg: 50%,  $\leq 10$  mmHg: 83%,  $\leq 15$  mmHg: 89% for MBP. Based on these results, this framework satisfies the requirements for Grade C according to the BHS classification. Compared with multivariate MS- or MW-PTT for BP regression, MS-PTT achieves  $\leq 5$  mmHg: 41% for SBP, 50% for DBP, and 46% for MBP; MW-PTT shows  $\leq 5$  mmHg: 40% for SBP, 48% for DBP, and 46% for MBP in MLR subject-dependent setting. The BP estimation results from MS+MW-PTT present a slight improvement (about 4%-7%) than only using MS-PTT or MW-PTT. In addition, multivariate PAT using RFR model also achieves a good result, showing  $\leq 5$  mmHg: 52% for SBP, 56% for DBP, and 64% for MBP.

In the subject-independent SVR setting, MS+MW-PTT illustrates better results according to the BHS standard compared to other settings. The cumulative coverage rates is shown below:  $\leq 5$  mmHg: 54%,  $\leq 10$  mmHg: 84%,  $\leq 15$  mmHg: 95% for SBP;  $\leq 5$  mmHg: 51%,  $\leq 10$  mmHg: 79%,  $\leq 15$  mmHg: 92% for DBP;  $\leq 5$  mmHg: 44%,  $\leq 10$  mmHg: 84%,

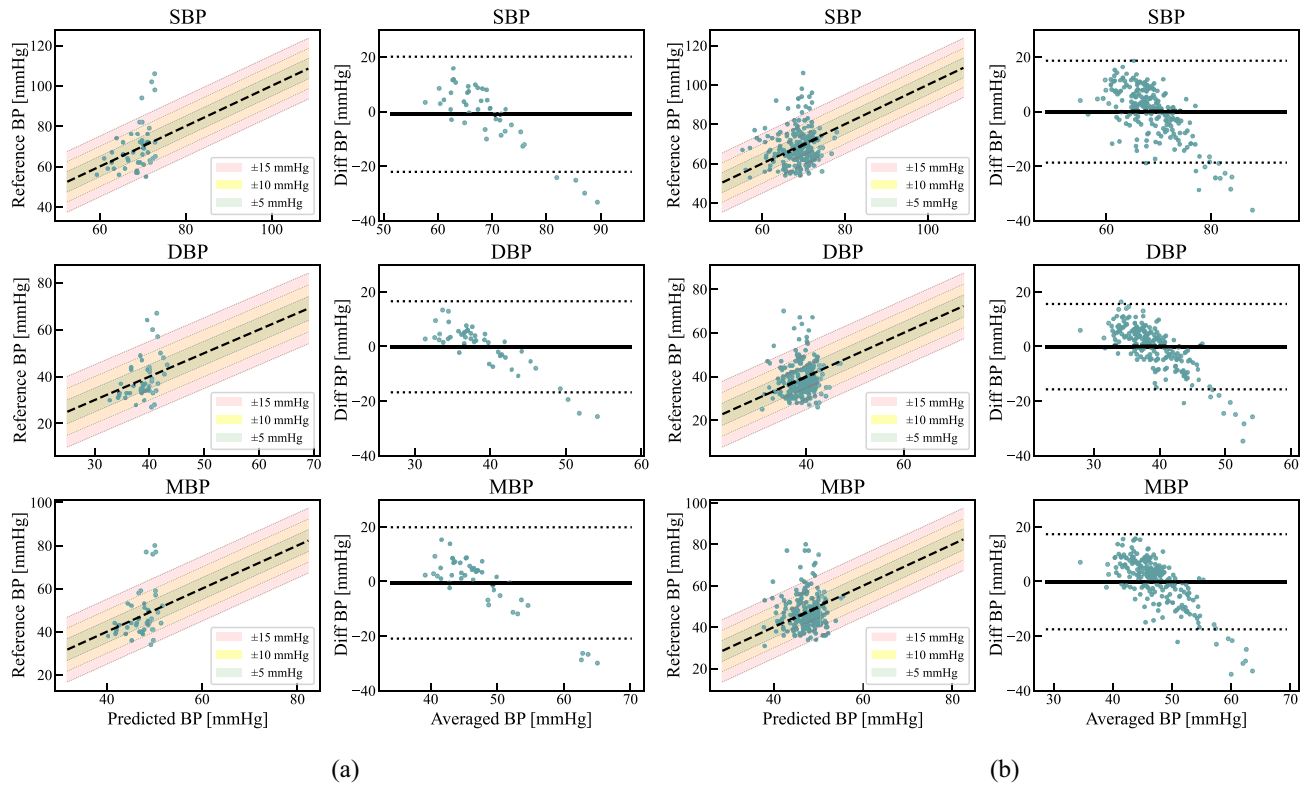


Fig. 7. This figure presents the correlation scatter plots and Bland–Altman plots for BP estimation using the MS+MW-PTT MLR model. The left panel (a) depicts subject-dependent measurements, while the right panel (b) illustrates subject-independent measurements. The correlation scatter plots include BHS standard error bands of  $\pm 5$  mmHg,  $\pm 10$  mmHg, and  $\pm 15$  mmHg.

$\leq 15$  mmHg: 94% for MBP. It almost satisfied the grade B of the BHS standard, except for the  $MBP \leq 5$  mmHg. Because of the narrow range of BP data in our dataset, SBP primarily between 60–80 mmHg, DBP between 35–45 mmHg, and MBP between 40–55 mmHg (as shown in Fig. 3) with relatively few instances of high BP, accurate BP estimation out of this range is particularly challenging (as shown in Fig. 7). This limited range reduces the variability in BP values, and also affects the overall PCC values (as shown in Table VI). Therefore, expanding our dataset in future studies to include a broader range of BP values, particularly more data points in the hypertensive range, is essential. This would allow for a more comprehensive evaluation of the relationship between PTT and BP.

#### D. Limitations and Future Works

This proof-of-concept study is the first attempt to measure BP in neonates using a combination of MS-PTT and MW-PTT. This is a significant step forward in understanding the feasibility and challenges of measurement on this population. We demonstrated the feasibility of this approach, including hardware setups and algorithms, even under the challenging conditions associated with neonatal physiology and signal acquisition. By combining MS-PTT and MW-PTT, we provided a new perspective on improving the accuracy of camera-based contactless BP estimation in neonates. Our work lays the foundation for developing population-specific models and methodologies, addressing a critical gap in BP monitoring

from the adult population to the neonatal population. These results also suggest promising methods for future work and highlight some limitations to consider.

This proof-of-concept study was conducted on a relatively small sample size of 40 neonates, and a larger dataset would enhance the generalizability of the findings. In the next step, we will organize multicenter clinical trials to include more infants from NICUs of different hospitals, to create a dataset with a larger and more diverse population of neonates to improve the model's generalizability. For subject-dependent models, the limited monitoring duration (10–30 minutes per neonate) restricts the ability to evaluate the model's effectiveness in tracking BP over longer periods, which is essential for practical deployment. Future studies should aim to extend the monitoring duration to address this limitation.

A limitation of MS-PTT is the difficulty in consistently selecting the exact same skin region for long-term BP monitoring, as factors, such as coverings (e.g., bed sheets or tissues). We could explore the option of incorporating robust body-part segmentation algorithms specifically designed for the NICU environment to address this challenge [50], [51].

One limitation of MW-PTT is that the overlap between wavelengths in different channels may be suboptimal for MW-PTT measurement. This overlap can be mitigated by incorporating narrow-band optical filters during optical signal acquisition to achieve better channel separation [19]. However, narrow-band filters may significantly reduce the amount of photons received by the sensor and thus lead to low signal-to-noise ratio (SNR). Polarization techniques can enhance skin

layer segmentation. This is because polarized light photons with longer wavelengths, like red light (R), penetrate deeper into the skin and experience greater depolarization compared to those with shorter wavelengths, such as green (G) and blue (B) light [52].

Exploitation of additional morphological features derived from the MW-rPPG signal might further improve the accuracy of contactless BP estimation [25], [53]. Cardiac output features (e.g., ascending and descending time) and peripheral resistance features (e.g., PIR, ascending slope, and descending slope) can be extracted from rPPG signals [53]. The augmented index of PPG, associated with arterial compliance and stiffness related to BP [54], may be calculated using two different wavelengths of rPPG signals [25]. In addition, BP and HRV are closely related, reflecting underlying autonomic regulation mechanisms [55]. In preterm neonates, Semenova et al. [56] demonstrated that HRV features can predict short-term neurological outcomes, particularly during episodes of low MBP. Combining PTT and HRV features measured by a camera may further improve the accuracy of BP monitoring by providing a more comprehensive view of cardiovascular regulation. By addressing these limitations in future work, there is a hope to develop reliable methods for noncontact and continuous neonatal BP assessment.

## V. CONCLUSION

This study investigates a contactless approach for neonatal BP estimation using camera-based rPPG signals. The rPPG signal was acquired from the neonatal head, hand, and legs. We calculated multiple PTT features: MS-PTT for head-leg (right and left) and hand-leg (right and left) measurements, and MW-PTT derived from RGB signals measured from the neonatal head. Additionally, PAT was calculated based on the time delay between the ECG R-peak and three contact-PPG morphological features (peaks, feet, and maximum first derivative) as a benchmarking candidate. These PTT and PAT features were evaluated for BP estimation using both univariate and multivariate approaches. Combining MS-PTT and MW-PTT yielded the best results, achieving an  $MAE \pm STD$  of  $7.65 \pm 7.48$  mmHg for SBP,  $6.31 \pm 5.58$  mmHg for DBP, and  $7.29 \pm 7.29$  mmHg for MBP, based on MLR subject-dependent modeling. The proposed framework (MS+MW-PTT, MLR model) achieves the following cumulative coverage rates according to the BHS guidelines:  $\leq 5$  mmHg: 48%,  $\leq 10$  mmHg: 76%,  $\leq 15$  mmHg: 89% for SBP;  $\leq 5$  mmHg: 54%,  $\leq 10$  mmHg: 85%,  $\leq 15$  mmHg: 91% for DBP;  $\leq 5$  mmHg: 50%,  $\leq 10$  mmHg: 83%,  $\leq 15$  mmHg: 89% for MBP. According to the BHS guidelines, these results meet the requirements for Grade C. These findings provide preliminary validation of using MS-PTT and MW-PTT features for contactless neonatal BP estimation. In future research, we shall address practical challenges in NICU to make BP monitoring more robust to body motions, lighting changes, and subject-independent modeling. Additionally, we aim to further elucidate the relationship between camera-based PTT features and other pulse wave parameters.

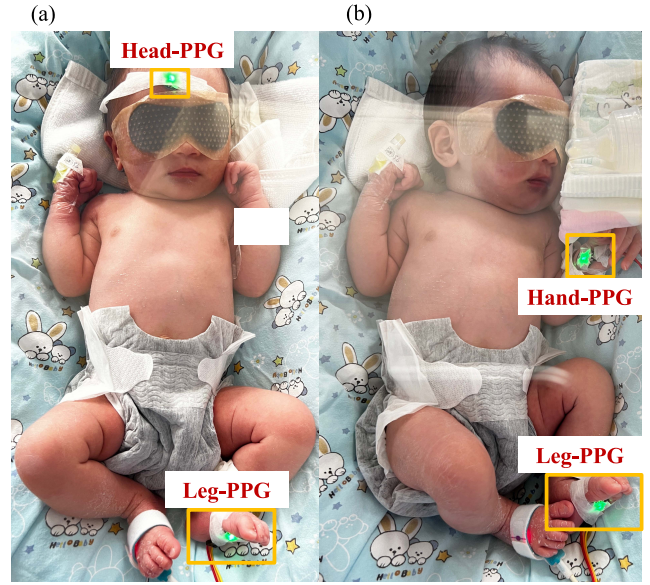


Fig. 8. Contact-PPG measurement setup. One PPG sensor is attached to the head/hand, and the other is attached to the leg.

## APPENDIX

### A. Contact-Based MS-PTT

We conducted additional analyses and experiments using two contact-based PPG sensors, focusing on a more deterministic proof-of-concept study of MS-PTT in BP calibration. Specifically, we measured two contact-based PPG signals (i.e., one attached to the head/hand and the other attached to the leg) to calculate contact-based MS-PTT (as shown in Fig. 8). The contact-based PPG signals were simultaneously triggered by the computer, with timestamps recorded for precise synchronization. The PPG signals were sampled at a rate of 100 Hz. Due to the thin skin of neonates, the quality of the contact-based PPG waveforms was relatively high (as shown in Fig. 9), and no signal filtering was applied. The results indicate that the contact-based PTT between the head and leg is 55 and 16 ms, while the PTT between the hand and leg is 44 and 17 ms, depending on individual variations (as shown in Fig. 9). The results are generally consistent with the theoretical estimates but are slightly lower than the predicted values. This discrepancy may be attributed to the specific measurement sites in the experiment, individual vascular characteristics, and variations in actual arterial path lengths. The camera-based MS-PTT values are generally within the range of 13–44 ms, which is similar to contact-based MS-PTT values.

### B. SNR of rPPG Signals

We have conducted a comprehensive analysis of the SNR of rPPG signals extracted from different body parts, including the head, hands, and legs. In Table VIII, we present the averaged SNR of rPPG signals from different body parts. The ratio of signal power to noise power provided SNR according to the formula

$$SNR = 10 \cdot \log_{10} \left( \frac{\sum_{f=1.5}^4 (U_t(f)S(f))^2}{(1 - U_t(f)S(f))^2} \right) \quad (4)$$

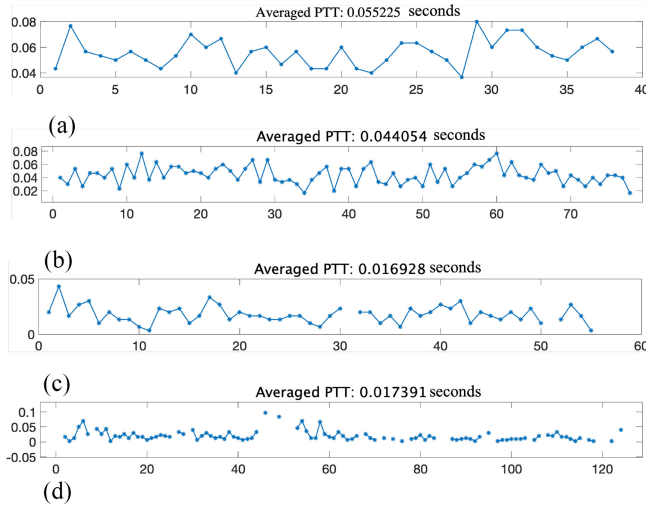


Fig. 9. PTT was calculated using contact-based PPG signals. (a) Head-Leg from Infant 1; (b) Hand-Leg from Infant 1; (c) Head-Leg from Infant 2; (d) Hand-Leg from Infant 2.

TABLE VIII  
AVERAGE SNR OF rPPG FROM DIFFERENT BODY PARTS

mean snr (dB)	Left hand	Right hand	Left leg	Right leg	Head (red)	Head (green)	Head (blue)
mean snr (dB)	6.81	7.69	6.36	6.77	8.12	12.64	6.85

where  $S(f)$  is the spectrum of the signal,  $f$  is the frequency (Hz), and  $U_t(f)$  is a binary window to pass the pulse frequency and isolate the noise frequency.

The mean SNR of rPPG signals extracted from the head is 12.64 dB, while the mean SNR of rPPG signals extracted from the hands and legs is between 6.36 and 7.69 dB. Although the SNR of rPPG signals extracted from the hands and legs is lower than that from the head, the mean SNR remains sufficiently high to support the calculation of MS-PTT. Similarly, while the blue channel's SNR is lower than that of the green channel, it achieves an average SNR of 6.85 dB, which is adequate for MW-PTT calculation and supports its feasibility (as shown in Table VIII).

## REFERENCES

- J. E. Jones and P. A. Jose, "Neonatal blood pressure regulation," *Seminars Perinatol.*, vol. 28, no. 2, pp. 141–148, Apr. 2004.
- J. R. Evans, B. L. Short, K. V. Meurs, and H. C. Sachs, "Cardiovascular support in preterm infants," *Clin. Therapeut.*, vol. 28, no. 9, pp. 1366–1384, Sep. 2006.
- H. Wang, J. Huang, G. Wang, H. Lu, and W. Wang, "Contactless patient care using hospital IoT: CCTV-camera-based physiological monitoring in ICU," *IEEE Internet Things J.*, vol. 11, no. 4, pp. 5781–5797, Feb. 2024.
- S. Meyer, J. Sander, S. Gräber, S. Gottschling, and L. Gortner, "Agreement of invasive versus non-invasive blood pressure in preterm neonates is not dependent on birth weight or gestational age," *J. Paediatr. Child Health*, vol. 46, no. 5, pp. 249–254, May 2010.
- J. M. Dionne et al., "Method of blood pressure measurement in neonates and infants: A systematic review and analysis," *J. Pediatrics*, vol. 221, pp. 23–31, Jun. 2020.
- P. A. Obrist, K. C. Light, J. A. McCubbin, J. S. Hutcheson, and J. L. Hoffer, "Pulse transit time: Relationship to blood pressure," *Behav. Res. Methods Instrum.*, vol. 10, no. 5, pp. 623–626, Sep. 1978.
- W. Chen, T. Kobayashi, S. Ichikawa, Y. Takeuchi, and T. Togawa, "Continuous estimation of systolic blood pressure using the pulse arrival time and intermittent calibration," *Med. Biol. Eng. Comput.*, vol. 38, no. 5, pp. 569–574, Sep. 2000.
- C. Poon and Y. Zhang, "Cuff-less and noninvasive measurements of arterial blood pressure by pulse transit time," in *Proc. IEEE Eng. Med. Biol. 27th Annu. Conf.*, Shanghai, China, 2005, pp. 5877–5880.
- H. Gesche, D. Grosskurth, G. Küchler, and A. Patzak, "Continuous blood pressure measurement by using the pulse transit time: Comparison to a cuff-based method," *Eur. J. Appl. Physiol.*, vol. 112, no. 1, pp. 309–315, Jan. 2012.
- X.-R. Ding and H. K. Tsang, "Continuous cuffless blood pressure estimation using pulse transit time and photoplethysmogram intensity ratio," *IEEE Trans. Biomed. Eng.*, vol. 63, no. 5, pp. 964–972, May 2016.
- C.-S. Kim, A. M. Carek, R. Mukkamala, O. T. Inan, and J.-O. Hahn, "Ballistocardiogram as proximal timing reference for pulse transit time measurement: Potential for cuffless blood pressure monitoring," *IEEE Trans. Biomed. Eng.*, vol. 62, no. 11, pp. 2657–2664, Nov. 2015.
- Z. Chen, X. Yang, J. T. Teo, and S. H. Ng, "Noninvasive monitoring of blood pressure using optical ballistocardiography and photoplethysmograph approaches," in *Proc. 35th Annu. Int. Conf. IEEE Eng. Med. Biol. Soc. (EMBC)*, Osaka, Japan, Jul. 2013, pp. 2425–2428.
- Y. Oyamada et al., "Laser-based noncontact blood pressure estimation using human body displacement waveforms," in *Proc. IEEE/MTT-S Int. Microw. Symp.*, Denver, CO, USA, Jun. 2022, pp. 1020–1022.
- M. Golberg, J. Ruiz-Rivas, S. Polani, Y. Beiderman, and Z. Zalevsky, "Large-scale clinical validation of Noncontact and continuous extraction of blood pressure via multipoint defocused photonic imaging," *Appl. Opt.*, vol. 57, no. 7, p. B45, Mar. 2018.
- M. Liu, L.-M. Po, and H. Fu, "Cuffless blood pressure estimation based on photoplethysmography signal and its second derivative," *Int. J. Comput. Theory Eng.*, vol. 9, no. 3, pp. 202–206, 2017.
- W.-H. Lin, H. Wang, O. W. Samuel, G. Liu, Z. Huang, and G. Li, "New photoplethysmogram indicators for improving cuffless and continuous blood pressure estimation accuracy," *Physiol. Meas.*, vol. 39, no. 2, Feb. 2018, Art. no. 25005.
- D. Wang, X. Yang, J. Wu, and W. Wang, "Personalized modeling of blood pressure with photoplethysmography: An error-feedback incremental support vector regression model," *IEEE Internet Things J.*, vol. 11, no. 1, pp. 1732–1745, Jan. 2024.
- J. Liu, Y.-T. Zhang, X.-R. Ding, W.-X. Dai, and N. Zhao, "A preliminary study on multi-wavelength PPG based pulse transit time detection for cuffless blood pressure measurement," in *Proc. 38th Annu. Int. Conf. IEEE Eng. Med. Biol. Soc. (EMBC)*, Aug. 2016, pp. 615–618.
- G. Slapničar, W. Wang, and M. Luštrek, "Feasibility of remote blood pressure estimation via narrow-band multi-wavelength pulse transit time," *ACM Trans. Sensor Netw.*, vol. 20, no. 4, pp. 1–21, Jul. 2024.
- Y. Huang, D. Huang, J. Huang, H. Lu, M. He, and W. Wang, "Camera wavelength selection for multi-wavelength pulse transit time based blood pressure monitoring," in *Proc. 45th Annu. Int. Conf. IEEE Eng. Med. Biol. Soc. (EMBC)*, Jul. 2023, pp. 1–5.
- I. C. Jeong and J. Finkelstein, "Introducing contactless blood pressure assessment using a high speed video camera," *J. Med. Syst.*, vol. 40, no. 4, p. 77, Jan. 2016.
- X. Fan, Q. Ye, X. Yang, and S. D. Choudhury, "Robust blood pressure estimation using an RGB camera," *J. Ambient Intell. Human. Comput.*, vol. 11, no. 11, pp. 4329–4336, Nov. 2020.
- H. Luo et al., "Smartphone-based blood pressure measurement using transdermal optical imaging technology," *Circul., Cardiov. Imag.*, vol. 12, no. 8, Aug. 2019, Art. no. e00857.
- M. Jain, S. Deb, and A. V. Subramanyam, "Face video based touchless blood pressure and heart rate estimation," in *Proc. IEEE 18th Int. Workshop Multimedia Signal Process. (MMSP)*, Sep. 2016, pp. 1–5.
- G. Liao, H. Lu, C. Shan, and W. Wang, "Plethysmographic waveform features and hemodynamic features for camera-based blood pressure estimation," *IEEE Trans. Instrum. Meas.*, vol. 73, pp. 1–14, Dec. 2024.
- Y. Zeng et al., "Camera-based cardiorespiratory monitoring of preterm infants in NICU," *IEEE Trans. Instrum. Meas.*, vol. 73, pp. 1–13, Apr. 2024.
- Y. Zeng et al., "Camera-based monitoring of heart rate variability for preterm infants in neonatal intensive care unit," in *Proc. IEEE Int. Conf. E-Health Netw. Appl. Services (Healthcom)*, Dec. 2023, pp. 314–318.
- Y. Ye, D. Gu, and W. Wang, "Impact of different skin penetration depths of red and green wavelengths on camera-based SpO2 measurement," in *Proc. 45th Annu. Int. Conf. IEEE Eng. Med. Biol. Soc. (EMBC)*, Sydney, NSW, Australia, Jul. 2023, pp. 1–5.
- Y. Ye, L. Pan, D. Yu, D. Gu, H. Lu, and W. Wang, "Notch RGB-camera based SpO2 estimation: A clinical trial in a neonatal intensive care unit," *Biomed. Opt. Exp.*, vol. 15, no. 1, pp. 428–445, Jan. 2024.
- Y. Sun et al., "Respiration monitoring for premature neonates in NICU," *Appl. Sci.*, vol. 9, no. 23, p. 5246, Dec. 2019.

- [31] Y. Zeng, X. Song, J. Yang, and W. Wang, "Time-domain features of angular-velocity signals for camera-based respiratory ROI detection: A clinical study in NICU," in *Proc. 45th Annu. Int. Conf. IEEE Eng. Med. Biol. Soc. (EMBC)*. Sydney, NSW, Australia, Jul. 2023, pp. 1–6.
- [32] D. Huang, L. Ren, H. Lu, and W. Wang, "A scene adaption framework for infant cry detection in obstetrics," in *Proc. Annu. Int. Conf. IEEE Eng. Med. Biol. Soc.*, Jul. 2023, pp. 1–5.
- [33] Y. Sun et al., "Automatic and continuous discomfort detection for premature infants in a NICU using video-based motion analysis," in *Proc. 41st Annu. Int. Conf. IEEE Eng. Med. Biol. Soc. (EMBC)*. Berlin, Germany, Jul. 2019, pp. 5995–5999.
- [34] Y. Yuan et al., "A multi-Center clinical trial for camera-based infant sleep and awake detection in neonatal intensive care unit," in *Proc. IEEE Int. Conf. E-Health Netw., Appl. Services (Healthcom)*, Dec. 2023, pp. 319–322.
- [35] D. Huang et al., "Generalized camera-based infant sleep-wake monitoring in NICUs: A multi-Center clinical trial," *IEEE J. Biomed. Health Inform.*, vol. 28, no. 5, pp. 3015–3028, May 2024.
- [36] G. Slapnicar, W. Wang, and M. Lustrek, "Feasibility of remote pulse transit time estimation using narrow-band multi-wavelength camera photoplethysmography," in *Proc. IEEE-EMBS Int. Conf. Biomed. Health Inform. (BHI)*, Ioannina, Greece, Sep. 2022, pp. 1–5.
- [37] D. Shao, Y. Yang, C. Liu, F. Tsow, H. Yu, and N. Tao, "Noncontact monitoring breathing pattern, exhalation flow rate and pulse transit time," *IEEE Trans. Biomed. Eng.*, vol. 61, no. 11, pp. 2760–2767, Nov. 2014.
- [38] A. V. Moco, S. Stuijk, and G. De Haan, "New insights into the origin of remote PPG signals in visible light and infrared," *Sci. Rep.*, vol. 8, no. 1, p. 8501, May 2018.
- [39] Y. Huang et al., "Camera-based blood pressure monitoring based on multi-site and multi-wavelength pulse transit time features," *IEEE Trans. Instrum. Meas.*, vol. 73, pp. 1–14, Sep. 2024.
- [40] L. A. Geddes, M. H. Voelz, C. F. Babbs, J. D. Bourland, and W. A. Tacker, "Pulse transit time as an indicator of arterial blood pressure," *Psychophysiology*, vol. 18, no. 1, pp. 71–74, Jan. 1981.
- [41] R. Mukkamala et al., "Toward ubiquitous blood pressure monitoring via pulse transit time: Theory and practice," *IEEE Trans. Biomed. Eng.*, vol. 62, no. 8, pp. 1879–1901, Aug. 2015.
- [42] M. Yoshioka and S. Bouonyong, "Analysis of pulse transit time derived from imaging photoplethysmography and microwave sensor-based ballistocardiography," in *Proc. IEEE/CVF Conf. Comput. Vis. Pattern Recognit. Workshops (CVPRW)*, Seattle, WA, USA, Jun. 2020, pp. 1156–1162.
- [43] M. Kachuee, M. M. Kiani, H. Mohammadzade, and M. Shabany, "Cuffless blood pressure estimation algorithms for continuous health-care monitoring," *IEEE Trans. Biomed. Eng.*, vol. 64, no. 4, pp. 859–869, Apr. 2017.
- [44] R. A. Payne, C. N. Symeonides, D. J. Webb, and S. R. J. Maxwell, "Pulse transit time measured from the ECG: An unreliable marker of beat-to-beat blood pressure," *J. Appl. Physiol.*, vol. 100, no. 1, pp. 136–141, Jan. 2006.
- [45] G. Zhang, M. Gao, D. Xu, N. B. Olivier, and R. Mukkamala, "Pulse arrival time is not an adequate surrogate for pulse transit time as a marker of blood pressure," *J. Appl. Physiol.*, vol. 111, no. 6, pp. 1681–1686, Dec. 2011.
- [46] A. V. Moco, L. Z. Mondragon, W. Wang, S. Stuijk, and G. De Haan, "Camera-based assessment of arterial stiffness and wave reflection parameters from neck micro-motion," *Physiol. Meas.*, vol. 38, no. 8, pp. 1576–1598, Jul. 2017.
- [47] P. P. Lassalle et al., "Central pulse wave velocity in neonates: Feasibility and comparison to normative data," *Hypertension Res.*, vol. 43, no. 11, pp. 1322–1324, Nov. 2020.
- [48] D. Zhenjiang et al., "Comparative study of noninvasive blood pressure measurement of lateral position and supine position," *J. Basic Chin. Med.*, vol. 10, no. 9, pp. 59–60, 2004.
- [49] H. Shu, L. Ren, L. Pan, D. Huang, H. Lu, and W. Wang, "Single image based infant body height and weight estimation," in *Proc. IEEE/CVF Conf. Comput. Vis. Pattern Recognit. Workshops (CVPRW)*, Jun. 2023, pp. 6052–6059.
- [50] Y. Zeng et al., "Video-based body parsing for neonatal body-parts actigraphy: A clinical study in NICU," in *Proc. 46th Annu. Int. Conf. IEEE Eng. Med. Biol. Soc. (EMBC)*, Orlando, FL, USA, Jul. 2024, pp. 1–4.
- [51] H. Ni, Y. Xue, L. Ma, Q. Zhang, X. Li, and X. Huang, "Semi-supervised body parsing and pose estimation for enhancing infant general movement assessment," *Med. Image Anal.*, vol. 83, Jan. 2023, Art. no. 102654.
- [52] W. Wang, H. Shu, H. Lu, M. Xu, and X. Ji, "Multispectral depolarization based living-skin detection: A new measurement principle," *IEEE Trans. Biomed. Eng.*, vol. 71, no. 6, pp. 1937–1949, Jun. 2024.
- [53] Z.-D. Liu et al., "Cuffless blood pressure measurement using smart-watches: A large-scale validation study," *IEEE J. Biomed. Health Inform.*, vol. 27, no. 9, pp. 4216–4227, Sep. 2023.
- [54] D. N. Dutt and S. Shruthi, "Digital processing of ECG and PPG signals for study of arterial parameters for cardiovascular risk assessment," in *Proc. Int. Conf. Commun. Signal Process. (ICCP)*, Apr. 2015, pp. 1506–1510.
- [55] G. Parati, J. P. Saul, M. D. Rienzo, and G. Mancia, "Spectral analysis of blood pressure and heart rate variability in evaluating cardiovascular regulation," *Hypertension*, vol. 25, no. 6, pp. 1276–1286, 1995.
- [56] O. Semenova, G. Carra, G. Lightbody, G. Boylan, E. Dempsey, and A. Temko, "Heart rate variability during periods of low blood pressure as a predictor of short-term outcome in preterms," in *Proc. 40th Annu. Int. Conf. IEEE Eng. Med. Biol. Soc. (EMBC)*, Honolulu, HI, USA, Jul. 2018, pp. 5614–5517.